

# SpikingGamma: Surrogate-Gradient Free and Temporally Precise Online Training of Spiking Neural Networks with Smoothed Delays

Roel Koopman<sup>1</sup> Sebastian Otte<sup>2</sup> Sander Bohté<sup>1</sup>

<sup>1</sup>Machine Learning Group, CWI <sup>2</sup>Institute of Robotics and Cognitive Systems, University of Lübeck  
 roel.koopman@cwi.nl sebastian.otte@uni-luebeck.de s.m.bohte@cwi.nl

## Abstract

Neuromorphic hardware implementations of Spiking Neural Networks (SNNs) promise energy-efficient, low-latency AI through sparse, event-driven computation. Yet, training SNNs under fine temporal discretization remains a major challenge, hindering both low-latency responsiveness and the mapping of software-trained SNNs to efficient hardware. In current approaches, spiking neurons are modeled as self-recurrent units, embedded into recurrent networks to maintain state over time, and trained with BPTT or RTRL variants based on surrogate gradients. These methods scale poorly with temporal resolution, while online approximations often exhibit instability for long sequences and tend to fail at capturing temporal patterns precisely. To address these limitations, we develop spiking neurons with internal recursive memory structures that we combine with sigma-delta spike-coding. We show that this SpikingGamma model supports direct error backpropagation without surrogate gradients, can learn fine temporal patterns with minimal spiking in an online manner, and scale feedforward SNNs to complex tasks and benchmarks with competitive accuracy, all while being insensitive to the temporal resolution of the model. Our approach offers both an alternative to current recurrent SNNs trained with surrogate gradients, and a direct route for mapping SNNs to neuromorphic hardware.

## 1 Introduction

Inspired by the brain, Spiking Neural Networks (SNNs) (Maass, 1997) hold promise for energy-efficient AI models (Li et al., 2023; Dampfhofer et al., 2022) as they use sparse and discrete spikes for communication and enable event-driven, asynchronous information processing. Spiking neurons can thus respond only when needed, achieving low-latency responsiveness while lowering energy consumption, especially when tasks exhibit extended temporal dynamics. Consequently, SNNs are well-suited for real-world tasks such as autonomous driving (Martínez et al., 2024), auditory signal processing (Baek & Lee, 2024), and drone control (Hagenaars et al., 2020). Treating spiking neurons as self-recurrent neural units and using a so-called Surrogate Gradient (SG) to backpropagate errors through the discontinuity of the spiking process (Neftci et al., 2019), current SNNs now demonstrate competitive performance with classical neural networks for small scale tasks (Hammouamri et al., 2024; Eshraghian et al., 2023).

Yet, as current SNNs are treated as time-stepped RNNs, they inherit many of the drawbacks of classical RNNs. This in particular include vanishing and exploding gradients, and the need to maintain or approximate past influences on current state to train these networks with algorithms like BPTT and RTRL (Zenke & Vogels, 2021) that incur prohibitive memory and/or timestep complexity. Online approximations to these algorithms have been developed (Kaiser et al., 2020; Wang et al., 2024), however, being approximations, they typically

fail when scaling either through time (sequence length) or space (network size), where the approximate nature of SGs compound these issues. In theory, SGs also intrinsically limit the degree of sparseness in a networks, as excessive sparsity amplifies gradient vanishing, collapsing training at a critical transition point (Zenke & Vogels, 2021).

There is a strong need however to be able to train SNNs over many timesteps, both to achieve low latency and also to enable efficient hardware implementations. For the latter, the deployment of SNNs in efficient hardware requires a careful correspondence between model network dynamics and actual dynamics of the physical substrates (Cramer et al., 2022; Ko et al., 2024; Koopman et al., 2025). As modeling actual physical dynamics is usually achieved via fine-grained temporal simulation, this requires the use of many small timesteps when training a hardware-compatible network (Ko et al., 2024). As noted however, this requirement conflicts with the current principal RNN-based SNN training paradigm, also, as we show, for online approximations to BPTT/RTRL like FPTT (Kag & Saligrama, 2021) and ES-D-RTRL (Wang et al., 2024).

Here, we introduce the SpikingGamma model and demonstrate how this model enables training over arbitrary fine temporal resolution. The model builds on earlier work including the Gamma-model (De Vries & Principe, 1992), the TKRNN (Sutskever & Hinton, 2010) and the Fractionally Predictive SNN (Bohte, 2011; Rombouts & Bohte, 2010). In the SpikingGamma model, spiking neurons internally employ adaptive recursive memory to efficiently create an increasingly

smoothed delayed representation of past inputs, where, as in (Yoon, 2016; Rombouts & Bohte, 2010), sigma-delta spike-coding then encodes the rectified internal state of the neuron into a spike-train, which is then effectively decoded at the received neuron – similar to pulsed sigma-delta coding in electrical circuits (Yoon, 2016). Combining adaptive recursive memory with sigma-delta spike-coding removes self-recurrency, and enables feedforward SNNs to be trained directly with error-backpropagation rather than BPTT, and without the use of SGs to overcome the spiking-discontinuity. Notably, thus formulated the networks can be trained with arbitrary temporal precision.

We show that thus formulated, the internal delays enable SpikingGamma spiking neurons to learn to detect the co-occurrence of temporally disjunct features, without externally maintaining memory through for example persistent activity. Discrete delays have been demonstrated to be highly effective for achieving high-performance in SNNs (Hammouamri et al., 2024). Ludvig et al. (2008) also already demonstrated that a smoothed-delay model can account for peculiarities of delayed-reward reinforcement learning in biology, where the prediction error response to a reward stimulus is directly suppressed when a reliable preceding cue-stimulus is learned. In their model, a stimulus generates a multitude of differentially delayed microstimuli affecting downstream neurons, enabling reinforcement learning to directly connect temporally disjunct stimuli and rewards. This model was however was not extended to multiple layers or to learn complex temporal tasks.

Here, we show how feedforward SpikingGamma SNNs can compete with state-of-the-art recurrent SNN approaches. We show that SpikingGamma SNNs can learn sparse and precise temporal coding over long timespans, while being insensitive to the temporal resolution of the simulated dynamics. We demonstrate this for both simple delay tasks, an echo-location task, and classical neuromorphic benchmarks like DVS Gesture, SHD and SSC where we show superior accuracy compared to current online methods with scalable temporal resolution. Our approach thus presents an alternative to current recurrent SNNs based on Surrogate Gradient training, where SpikingGamma SNNs can be trained and computed online and at arbitrarily high temporal resolution.

## 2 Related work

Where surrogate gradients have enabled training of SNNs with standard recurrent deep learning approaches, several alternatives to BPTT and RTRL have been explored to improve the training efficiency of SNNs. ANN-to-SNN conversion, while straightforward and scalable, fails to exploit the temporal dynamics and event-driven sparsity of SNNs, and most existing methods remain constrained to inefficient rate-based coding schemes (Zhou et al., 2024). Various approximations of RTRL and BPTT have been proposed that maintain temporal traces for credit assignment or regularize gradients through time rather than computing exact gradients, such as DECOLLE

(Kaiser et al., 2020), OSTL (Bohnstingl et al., 2022), OTPE (Summe et al., 2024), FPTT (Yin et al., 2023), OTTT (Xiao et al., 2022), and ES-D-RTRL (Wang et al., 2024). These methods have shown limited success on tasks demanding complex temporal reasoning. Another line of work seeks to exploit the inherent sparsity of SNN activity to reduce the memory footprint of BPTT, such as EventProp (Mészáros et al., 2025), though its scalability to large models and datasets remains unexplored.

Our work is inspired by a different idea: maintaining a compressed representation of history within the forward pass to enable temporal learning without requiring backpropagation through time. Related ideas have been explored in ANNs. For example, in the TKRNN (Sutskever & Hinton, 2010) all neurons are linked through all timesteps using a learned weight matrix, akin to delays, and WaveNet (Van Den Oord et al., 2016) uses dilated causal convolutions to model long-range temporal dependencies within a feedforward architecture, with performance comparable to LSTM-based RNNs. The Gamma Model (De Vries & Principe, 1992) similarly maintains adaptive internal memory to represent past inputs, functioning like a form of smoothed temporal convolution. Notably, so-called time-cells have been identified in the brain with similar delayed response properties (Liu et al., 2019), and Gamma-models have been proposed to account for internal dynamics in biological neurons such as spike-rate adaptation (Drew & Abbott, 2006). A related approach was applied to SNNs to avoid BPTT (Bohte, 2011), the delay-structure there however is incompatible with scalable learning as it cannot be computed in a recurrent manner – the concepts introduced in (De Vries & Principe, 1992) and (Bohte, 2011) however form the basis for our work.

## 3 Methods

### 3.1 The neuron model

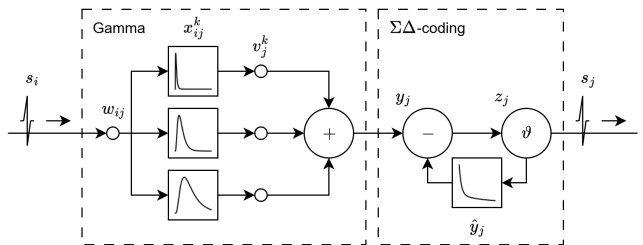


Figure 1: Overview of the neural processing model. At the synapses, incoming spikes generate weighted currents that evolve over multiple timescales. Within the neuron, the resulting synaptic responses are weighted according to their timescales and summed to produce a continuous neuronal signal. This signal is then converted back into spikes through  $\Sigma\Delta$ -coding, allowing downstream synapses to reconstruct an estimate of the original signal.

In the SpikingGamma model, we base the spiking neuron

model on a Linear-Non-Linear Sigma Delta (LNL-SD) temporal filtering model (Rombouts & Bohte, 2010), where a neuron  $j$  computes an internal signal  $y_j$  as the sum of the weighted and filtered inputs into the neuron. To implement sigma-delta spike-coding, the neuron additionally tracks a signal  $\hat{y}_j$  as the sum of spike-triggered refractory responses (Gerstner & Kistler, 2002): as in sigma-delta coding (Yoon, 2016), this sum of refractory responses approximates the rectified  $y_j$  by emitting a spike and adding a refractory response whenever the positive approximation error between  $\hat{y}_j$  and  $y_j$  exceeds a threshold  $\vartheta$  (Zambrano et al., 2019). The approximation of  $y_j$  is thus encoded by the spike-train determined by those threshold exceedances as downstream neurons can reconstruct the signal  $\hat{y}_j$  at their input – the neural processing model is illustrated in Figure 1. Mathematically, the signal  $y_j$  is computed as:

$$y_j(t) = \text{ReLU}(x_j(t)) \quad (1)$$

with  $x_j$  being the unrectified neuron signal. This is computed by filtering the synaptic input signals  $x_{ij}^k$  from neuron  $i$  to neuron  $j$  for  $k < K$  with each synapse having  $K$  temporal kernels. The filters can be instantiated as per-neuron or per-synapse. For per-neuron this is described as:

$$x_j(t) = \sum_k \sum_i x_{ij}^k(t) \cdot v_j^k, \quad (2)$$

where  $v_j^k$  is a parameter that weights the value of kernel  $k$  for neuron  $j$ . We refer to this as the “bucket weight”. The synaptic signal  $x_{ij}^k$  is then computed as:

$$x_{ij}^k(t) = \hat{y}_i^k(t) \cdot w_{ij}, \quad (3)$$

where  $w_{ij}$  is the synaptic weight, and  $\hat{y}_i^k$  is the temporal kernel  $k$  that estimates the signal of the upstream neuron  $i$ , as encoded by output spikes  $t_i$  from neuron  $i$  to  $j$ :

$$\hat{y}_i^k(t) = \sum_{t_i < t} \kappa^k(t - t_i), \quad (4)$$

where  $t_i$  denotes spike-times of neuron  $i$  up to time  $t$ , and  $\kappa^k$  being a set of temporal kernel functions implementing different delays.

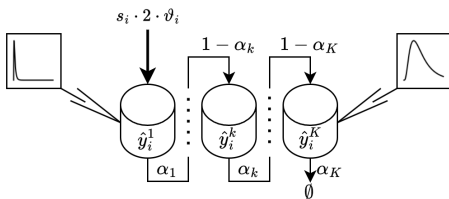


Figure 2: Visualization of temporal kernel computation using a cascade of leaky “buckets” that drain into one another at different rates ( $\alpha_k$ ). Each bucket represents a temporal kernel.

Following the Gamma-model (De Vries & Principe, 1992; Drew & Abbott, 2006) the kernels  $\kappa^k$  are computed as a series of “buckets” that spill over into each other. This is illustrated in Figure 2, and described as:

$$\hat{y}_i^k(t) = \begin{cases} \hat{y}_i^k(t-1)\alpha_k + s_i(t) 2 \vartheta_i(t), & k = 0, \\ \hat{y}_i^k(t-1)\alpha_k + \hat{y}_i^{k-1}(t-1)(1 - \alpha_k), & k > 0. \end{cases} \quad (5)$$

with  $\alpha_k$  specifying the transfer rate between buckets  $k$  and  $k-1$ ,  $\vartheta_i(t)$  being the threshold function of the spiking neuron, as defined in Section 3.3, and  $s_i(t) = 1$  if  $t \in \{t_i\}$  for an output spike-train  $\{t_i\}$ , else 0. The factor 2 ensures that  $\hat{y}$  matches the magnitude of  $y$  instead of being biased low (Zambrano et al., 2019). As this is a set of linearly coupled differential equations, each  $\hat{y}_i^k$  can be reformulated as Eq. (4) with each  $\kappa^k$  not relying on any other kernel: each  $\kappa^k$ , and thus each bucket  $\hat{y}_i^k$  can be modeled in a feedforward fashion without recurrency – that is, knowing the spike times of the inputs  $t_i < t$ , one can exactly compute the value of  $\hat{y}_i^k(t)$  for any  $t$  (Bohte, 2011).

Spike thresholding implements sigma-delta spike-coding (Yoon, 2016; Rombouts & Bohte, 2010) and is done by first computing a variable  $z_j(t)$  that is similar to the membrane potential by subtracting an approximation of the signal  $\hat{y}_j$ , which is what will be encoded by the to be emitted spikes, from the actual internal signal  $y_j$ :

$$z_j(t) = y_j(t) - \hat{y}_j(t-1), \quad (6)$$

with

$$\hat{y}_j(t) = \sum_k \hat{y}_j^k(t), \quad (7)$$

where  $\hat{y}_j^k$  is defined per Eq. (5) for the output of neuron  $j$  itself. When the difference exceeds a threshold, the signal approximation  $\hat{y}_j(t)$  is then updated by emitting a new spike:

$$\begin{aligned} s_j(t) &= z_j(t) > \vartheta_j(t), \\ t_j &= t, \quad \text{if } s_j(t) = 1 \end{aligned} \quad (8)$$

with  $\{t_j\}$  being the output spike-train. Figure 3 visualizes the complete forward path together with example signal values at each stage.

Importantly, thus formulated both the signal approximation at the output of the neuron and the signal received at the downstream synapses are actually the same. This makes it possible to directly use  $\hat{y}_j^k(t)$  for computations at those downstream synapses (i.e., for Eq. (3)). To filter per synapse, the only change needed to the model above is to use individual per-synapse bucket weights  $v_{ij}^k$  instead of  $v_j^k$ .

### 3.2 Error-backpropagation

For classification, given some desired output label  $y_{\text{true}}(t)$  and the actual neuron signal of the output neuron  $y_{\text{out}}(t)$ , we compute a loss such as the Cross-Entropy (CE) loss  $L(t) = L^{\text{CE}}(y_{\text{out}}(t), y_{\text{true}}(t))$ , evaluated independently at each discrete timestep, since temporal credit assignment is handled explicitly via bucketed histories rather than recurrent state (see Figure 4). If the task requires a precise spike timing, we instead use a Mean Squared Error (MSE) loss between the

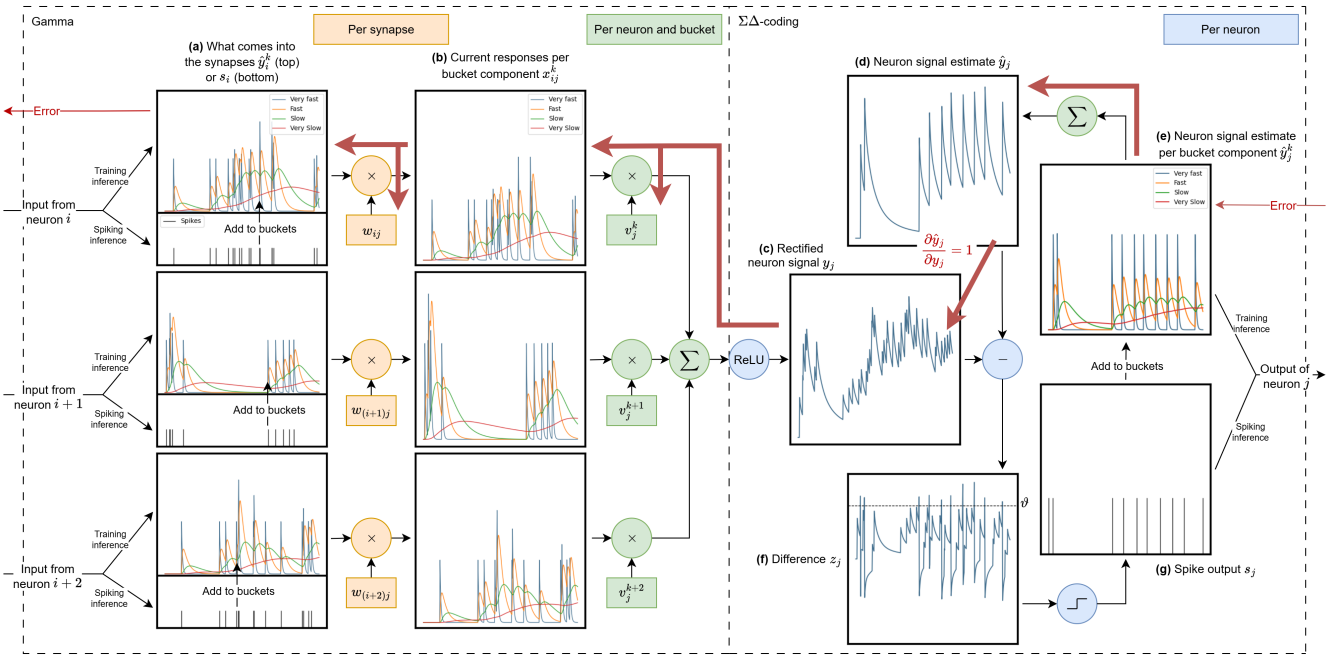


Figure 3: Signal evolution and error propagation in the neuron model. (a) At each input synapse, the neuron receives a signal. During training this is the signal estimate  $\hat{y}_i^k$  of the presynaptic neuron, while during spiking inference (e.g., on a neuromorphic chip) this estimate is reconstructed from the incoming spike train  $s_i$  following Eq. (5). (b) Each input is scaled by its synaptic weight  $w_{ij}$ , producing a current response per synapse and bucket. (c) These responses are weighted per bucket by the bucket weights  $v_j^k$  (or  $v_{ij}^k$  if weighted on synapse level), then accumulated across the buckets and finally rectified, forming the neuron signal  $y_j$ . (d) For discretizing this analog signal back into spikes, the neuron maintains a running estimate  $\hat{y}_j$  that is encoded by the output spikes. (e) This estimate is expressed in the same kernel basis as the input, ensuring consistency across layers. Because  $\hat{y}_j^k$  is mathematically identical to the input representation  $\hat{y}_i^k$  (Eq. (5)), it can be passed directly to downstream synapses during training, without spike decoding. (f) As in sigma-delta coding, whenever the mismatch  $z_j = y_j - \hat{y}_j$  exceeds a threshold, a correction is triggered. (g) This results in a spike output  $s_j$ , which is added back into the estimate. The red arrows indicate the error pathway during training: the error flows from the signal estimate back to the neuron signal and further to the inputs and parameters. Notably, the error bypasses the spikes, eliminating the need for surrogate gradients.

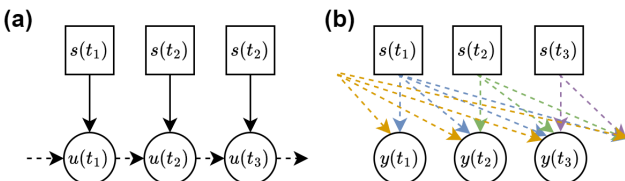


Figure 4: Transition of neuron states over time in recurrent architectures (a) versus SpikingGamma (b). Recurrent models rely on internal states (e.g., membrane potential  $u$ ) and therefore require BPTT for training, while SpikingGamma has access to the entire history via buckets for each timestep and so does not need BPTT.

expected  $\hat{y}_{\text{true}}(t)$  that would follow from a spike in the correct class at the right time, and actual neuron output  $\hat{y}_{\text{out}}(t)$ . Then,  $L(t) = L^{\text{MSE}}(\hat{y}_{\text{out}}(t), \hat{y}_{\text{true}}(t))$ .

As illustrated in Figure 3, for each discrete timestep  $t$ , we use the variables at that timestep to compute the loss with respect to the synaptic weights  $w_{ij}$  and the bucket weights  $v_j^k$  (or  $v_{ij}^k$  in the case of per-synapse filtering) (we omit the

explicit time index ( $t$ )):

$$\frac{\partial L}{\partial w_{ij}} = \frac{\partial L}{\partial \hat{y}_j} \frac{\partial \hat{y}_j}{\partial y_j} \frac{\partial y_j}{\partial x_j} \sum_k \frac{\partial x_j}{\partial x_{ij}^k} \frac{\partial x_{ij}^k}{\partial w_{ij}}, \quad (9)$$

$$\frac{\partial L}{\partial v_j^k} = \frac{\partial L}{\partial \hat{y}_j} \frac{\partial \hat{y}_j}{\partial y_j} \frac{\partial y_j}{\partial x_j} \frac{\partial x_j}{\partial v_j^k}, \quad (10)$$

where  $\frac{\partial L}{\partial \hat{y}_j}$  follows directly from the definition of the loss function. To avoid having to backpropagate through spikes, we exploit the definition of  $\hat{y}_j$  as being an approximation of  $y_j$ , thus having  $\frac{\partial \hat{y}_j}{\partial y_j} = 1$ .

The other terms follow directly from their forward pass, namely:  $\frac{\partial y_j}{\partial x_j} = \text{ReLU}'(x_j)$ ,  $\frac{\partial x_j}{\partial x_{ij}^k} = v_j^k$ , and finally  $\frac{\partial x_{ij}^k}{\partial w_{ij}} = \hat{y}_i^k$  and  $\frac{\partial x_j}{\partial v_j^k} = \sum_i x_{ij}^k$  (again, replace  $v_j^k$  with  $v_{ij}^k$  for per synapse filtering). To traverse the computational tree over a layer, the last term of Eq. (9) is replaced with  $\frac{\partial x_{ij}^k}{\partial \hat{y}_i} = w_{ij}$ .

### 3.3 Initialization, regularization and constraints

Before training, parameters are initialized. During training, we apply regularization and add constraints to prevent overfitting, improve model generalization, and increase sparsity. We use standard methods as summarized below, and additionally describe our *Adaptive Thresholding* and *Bucket-transfer Rate Initialization* in detail.

**Dropout on neuron signal.** Randomly zero out the neuron signal  $y$  with a given probability during training. The decision to drop is independent according to a Bernoulli distribution. Applied to every layer except the output layer.

**Layer normalization.** Normalizes the neuron signal before rectification ( $x$ ) based on layer statistics (Ba et al., 2016):  $x_{\text{norm}} = \frac{x - \text{E}[x]}{\sqrt{\text{Var}[x] + \epsilon}} \cdot \gamma + \beta$ , with  $\gamma$  the gain,  $\beta$  the bias (both trainable), and  $\text{E}[x]$  and  $\text{Var}[x]$  respectively the mean and variance of the neuron signal over all neurons in the layer.

**Gain loss.** Penalizes the magnitude of the gain term  $\gamma_l$  of the normalization layers:  $L_{\text{gain}} = G \cdot \sum_l \gamma_l$ , where  $G$  is a constant that affects the relative importance of the gain loss term, and  $l$  is the normalization layer index. This shrinks the signal, in turn reducing the number of spikes.

**Weight initialization.** Synaptic weights and biases on fully-connected and convolutional layers are sampled from  $\mathcal{U}(-\sqrt{k}, \sqrt{k})$  with  $k = \frac{1}{\text{input features}}$ . The bucket weights are sampled from  $\mathcal{N}(0, 0.1)$ .

**Adaptive thresholding.** In the sigma-delta spike-coding model, whenever the difference between  $y$  and  $\hat{y}$  exceeds a fixed threshold, a constant input  $s$  (pulse) is added to  $\hat{y}$ . As  $y$  increases, the leak from the buckets (which grows relative to  $\hat{y}$ ) eventually balances this constant input. Beyond that point, if  $y$  reaches an even higher value, the leak will prevent  $\hat{y}$  from approaching  $y$ . Consequently, the relation  $\frac{\partial \hat{y}}{\partial y} = 1$  no longer holds, which can disrupt training.

To overcome this, we use an adaptive thresholding mechanism (Zambrano et al., 2019) that increases the threshold, and therefore the amount added to the buckets, in proportion to  $\hat{y}(t-1)$ :

$$\vartheta(t) = \vartheta_0 + \hat{y}(t-1) \cdot m_f \quad (11)$$

where  $\vartheta_0$  is the minimum threshold, and  $m_f$  is a constant scaling factor. In our experiments, we set  $m_f = \vartheta_0$ . With this adaptive thresholding,  $\hat{y}$  can approximately track any positive value of  $y$  (Figure A2 Appendix). As the adaptive threshold can be calculated at the receiving neuron side, binary spikes can still be used, or graded spikes absent such downstream calculation (Zambrano et al., 2019).

**Bucket transfer rate initialization.** Following (Bohte, 2011), we ensure that the combined sum of buckets follows a power-law-like curve to facilitate learning long-range temporal filtering. To achieve this, we generate linearly separated values  $l_k \in \text{linspace}(L_{\text{start}}, L_{\text{end}}, K)$ , with  $L_{\text{start}} \in (0, 1)$  being the starting value,  $L_{\text{end}} \in (0, 1)$  being the final value (both included in the generated value range), and  $K$  the number of

values, one for each bucket. This is then used to compute the transfer rates,

$$\alpha_k = (l_k)^F, \quad (12)$$

with  $F \in (0, 1)$  being the transfer rate factor. Combined with  $L_{\text{start}}$ ,  $L_{\text{end}}$ , and  $K$  this determines the shape of the curve. For all experiments,  $L_{\text{start}} = 0.1$  and  $L_{\text{end}} = 0.9$ . In Table A5 (Appendix), the neuron response for different values of  $F$  are shown.

## 4 Experiments and results

We demonstrate how deep feedforward SpikingGamma SNNs can (1) learn to detect and respond to precisely timed spikes, with minimal spiking, (2) achieve accuracy in temporally sensitive benchmarks competitive and exceeding current online learning approaches for SNNs, and, (3) scale without loss of accuracy to fine-temporal resolutions which are infeasible with exact recurrent learning and where current approximate online learning approaches fail.

### 4.1 Learning exact timings through delayed responses

We demonstrate the ability of SpikingGamma to efficiently learn to detect fine temporal structure in two examples involving temporally structured computations.

**Learning delays.** In the first task, a single input spike needs to be propagated with a precise delay through a hidden neuron to a single output neuron. This task allows us to compare BPTT learning with BP learning in the feedforward SpikingGamma model.

Specifically, an input is provided at  $t = 0$ , and the network is trained to produce an output at  $t = 150$ . Each of the two trainable layers in the network contains a single neuron, with only the bucket weights being trainable while the synaptic weights between input and hidden, and hidden and output neuron remain fixed. We compute the MSE loss between the actual output and expected output per timestep. We define output per the trace  $\hat{y}$  that follows from the spike output.

For BPTT with SGs, the gradient is computed as:

$$\begin{aligned} \frac{\partial L}{\partial v_j^k} &= \frac{\partial L}{\partial \hat{y}_j(t)} \frac{\partial \hat{y}_j(t)}{\partial s_j(t)} \frac{\partial s_j(t)}{\partial z_j(t)} \frac{\partial z_j(t)}{\partial y_j(t)} \frac{\partial y_j(t)}{\partial x_j(t)} \\ &\times \left( \sum_{t' < t} \frac{\partial x_j(t)}{\partial x_j(t')} \frac{\partial x_j(t')}{\partial v_j^k} + \frac{\partial x_j(t)}{\partial v_j^k} \right). \end{aligned} \quad (13)$$

BPTT propagates back through the spikes via an SG  $z_j$  and then back in time through the buckets, rather than treating the system as feedforward as in the SpikingGamma model.

In Figure 5, we plot for both methods the neuron signal dynamics after training (on the left), and how the bucket weights evolved during training (on the right). Both approaches succeed in learning the long delay. However, the SpikingGamma SNN can precisely target delay kernels at the timesteps where

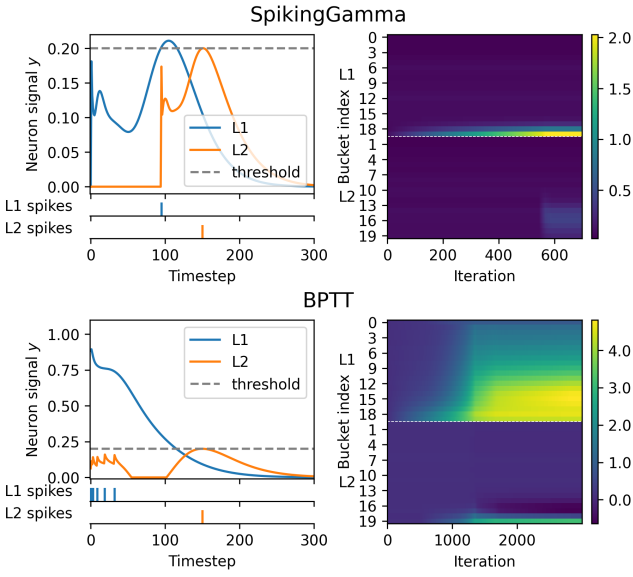


Figure 5: Comparison between SpikingGamma (top) and BPTT with SGs (bottom). Left shows the neuron dynamics after converging, and right the bucket-weight evolution during training.

signal increases should occur, allowing it to realize the delay with minimum spikes (two), whereas BPTT with SGs reinforces a broader band of kernels, an effect that may reflect diffuse temporal credit assignment and the smooth surrogate derivative spreading gradients across nearby timesteps, consistent with (Li et al., 2024).

**Learning delayed coincidence detection.** In the second task, illustrated in Figure 6, the goal is to learn delayed coincidence detection. Here, a sound arriving from a particular direction is represented by a distinct pair of spike times across two input channels, where the class is determined by the relative time-difference between the two spikes. This mimics the mechanism used by barn owls to localize prey based on subtle interaural time differences in the arrival time of spikes as a function of azimuth of the prey relative to the owl’s head direction (Carr & Konishi, 1990).

The input consists of a spike pair (left (L) spike time, right (R) spike time) as defined by the class, plus jitter drawn from  $\text{Uniform}(0, 2)$ . For the four classes, the pairs are: (4, 60), (4, 20), (20, 4), and (60, 4). The target for each class is a single output spike at time 200 from the corresponding class neuron, with other output neurons remaining silent (see Figure 6b). The loss is computed the same way as for learning delays. Both the left and right input have their own unique synaptic connections to all four output neurons (so 8 connections in total), thus each output neuron has two synaptic inputs (see Figure 6a). Each of these synapses has 25 buckets, where the bucket weights are trainable and applied on synapse level. Within each neuron, the synaptic responses of both inputs are summed up.

Figure 6c shows the synaptic responses after training. Effec-

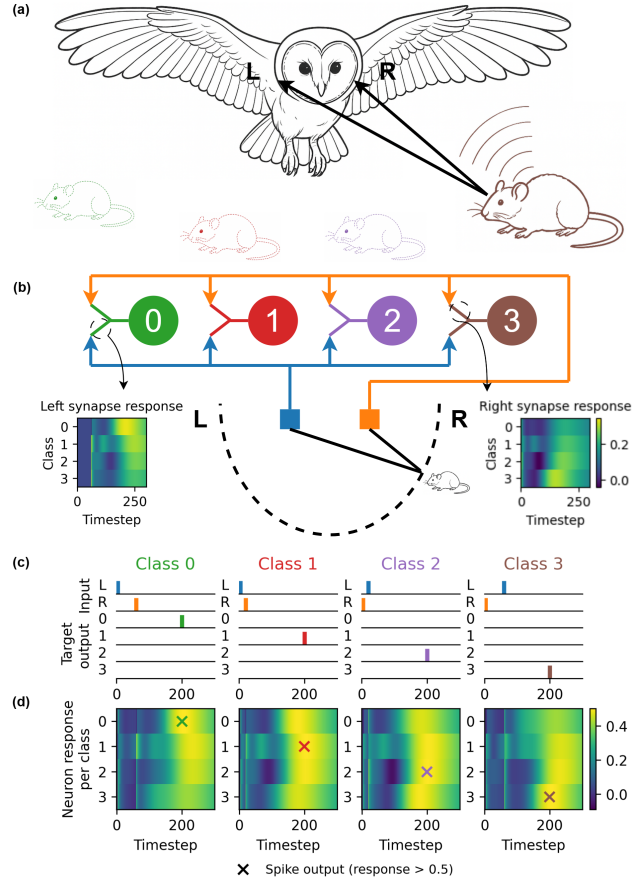


Figure 6: (a) An owl detects sound waves emitted by a target, such as moving prey, and these waves reach each ear at slightly different times. This difference in travel distance creates an interaural time difference, which the owl uses to accurately determine the prey’s position in the horizontal plane. (b) The architecture of the coincidence detection network, shown activated for a prey in the right-most (brown) position. The weighted bucket activations are shown for the left and right synapses of each class, with the left being more delayed. (c) Input and target spikes for all four classes. (d) Output neuron response to the correct class input as given in (c). Output spike (colored cross) is emitted at about  $t = 200$  in the correct class. Summing up the synaptic responses from (b) would result in Class 3 activation.

tively, each synapse learns a specific approximate delay such that for a specific pair of input spike times, their sum ( $L+R$ ) results in a spike for the right class at the right time (see Figure 6d). Accuracy (per time-to-first-spike coding) is 100% after training, with minimal spiking (maximal efficiency). This demonstration suggests that the SpikingGamma SNN is well suited for temporally structured classification tasks and aligned with biological neural coincidence detection.

## 4.2 Scaling through space and time

To demonstrate scaling to larger networks, problems and fine temporal resolution, we evaluate the SpikingGamma model on

Table 1: Comparison of online training methods for SNNs. SHD results for OTTT, OSTL, and OTPE are taken from (Summe et al., 2024), while the SHD result for DECOLLE is from (Quintana et al., 2024). All other results are taken from the original papers that introduced the respective methods. The architecture is given as [neurons in hidden layers ( $\times$  number of hidden layers)] if it is a sequence of fully connected layers, or provided in Section B.2.1 (Appendix) in detail if more complex. Results are reported as mean  $\pm$  std. Primary results correspond to test accuracy obtained after completing training. Values in parentheses indicate the peak test accuracy observed during training. We report both metrics, as peak test accuracy is generally considered unfair, but is still commonly reported and therefore added for comparison. A dash (-) indicates unavailable values. For reference, with BPTT (offline training), SE-adLIF achieves performance competitive with state-of-the-art methods, reaching  $93.79 \pm 0.76\%$  for SHD and  $80.44 \pm 0.26\%$  for SSC (Baronig et al., 2025).

Task	Frames	Method	Architecture	Accuracy $\pm$ std (peak)
DVS Gesture	1000	FPTT	2-layer FC, LTC	- ( $91.28 \pm 1.05$ )
	500	DECOLLE	4-layer CNN, CUBA LIF	- ( $95.54 \pm 0.16$ )
	2000	SpikingGamma	2-layer FC	<b><math>92.30 \pm 0.18</math> (<math>93.81 \pm 0.18</math>)</b>
	2000	SpikingGamma	4-layer CNN	<b><math>95.08 \pm 0.93</math> (<math>96.08 \pm 0.18</math>)</b>
SHD	50	OTTT	$[512 \times 3]$ , LIF	$71.2 \pm 0.8$ (-)
	50	OSTL	$[512 \times 3]$ , LIF	$70.6 \pm 0.7$ (-)
	50	OTPE	$[512 \times 3]$ , LIF	$75.4 \pm 0.5$ (-)
	100	DECOLLE	$[450]$ , ALIF	$62.01 \pm 0.61$ (-)
	100	ES-D-RTRL	$[1024 \times 3]$ , RadLIF	- ( $93.35 \pm 0.36$ )
	250	SpikingGamma	$[256 \times 3]$	<b><math>92.81 \pm 0.68</math> (<math>93.55 \pm 0.48</math>)</b>
SSC	250	SpikingGamma	$[512 \times 3]$	<b><math>75.63 \pm 0.44</math> (<math>75.91 \pm 0.54</math>)</b>

three widely used benchmarking datasets. We use DVS Gesture (Amir et al., 2017), SHD, and SSC (Cramer et al., 2020); while SHD and SSC can be handled with relatively shallow fully connected network topologies, they remain challenging because of the need to capture rich temporal dynamics. In contrast, DVS Gesture is less demanding temporally but has greater spatial complexity, for which we adopt both a shallow fully-connected and a deeper convolutional architecture. For SHD, we also include an ablation study to examine the effect of normalization, ReLU, and having a power-law shaped neuron response. Details of the experimental setup are provided in Section B (Appendix).

As noted, online training methods aim to perform temporal credit assignment without relying on BPTT or RTRL. However, depending on how traces or regularizers are formulated to approximate temporal gradients, existing approaches may fail to capture temporal dynamics accurately. To evaluate their impact on accuracy and enable a direct comparison with SpikingGamma SNNs, Table 1 reports our best results alongside those of prior online training methods. We include approaches that either provide results for training with a large number of frames (DVS Gesture) or report any results at all (SHD). To the best of our knowledge, no online baselines for SSC have been published. We distinguished methods that reported peak test accuracy during training as this can introduce mild test set leakage (Mészáros et al., 2025). To avoid this issue and improve reproducibility, we report final epoch test accuracy as well as peak accuracy.

As shown in Table 1, we find that SpikingGamma SNNs achieve highly competitive test accuracy across all datasets at superior temporal resolution. This is evident both in comparisons with FPTT and DECOLLE on DVS Gesture, and even

more so for SHD, where most other online methods struggle to achieve competitive performance. While DECOLLE performs well on DVS Gesture, it shows limited accuracy on SHD. For SHD, ES-D-RTRL is competitive provided just 100 input frames are used.

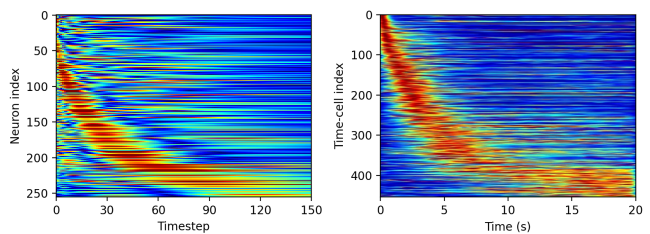


Figure 7: Comparison of neuron responses from our method with recorded rat time-cell activity. On the left: Neuron response for input at  $t = 0$  for neurons from the second hidden layer of the best performing model on SHD. Neuron indices sorted by peak activity timestep. On the right: Firing patterns of rats' time-cells during a temporal bisection task. Adapted from (Shimbo et al., 2021).

**Alignment with biological time-cell dynamics** To examine whether neurons in our model show time-cell-like dynamics, we analyzed the responses of neurons in a single layer to a single spike input after training on SHD. Comparing these neuronal responses to recorded biological time-cell activity revealed similar population dynamics. In both cases, the units activate sequentially over time with gradually decaying and temporally broadened responses, forming a characteris-

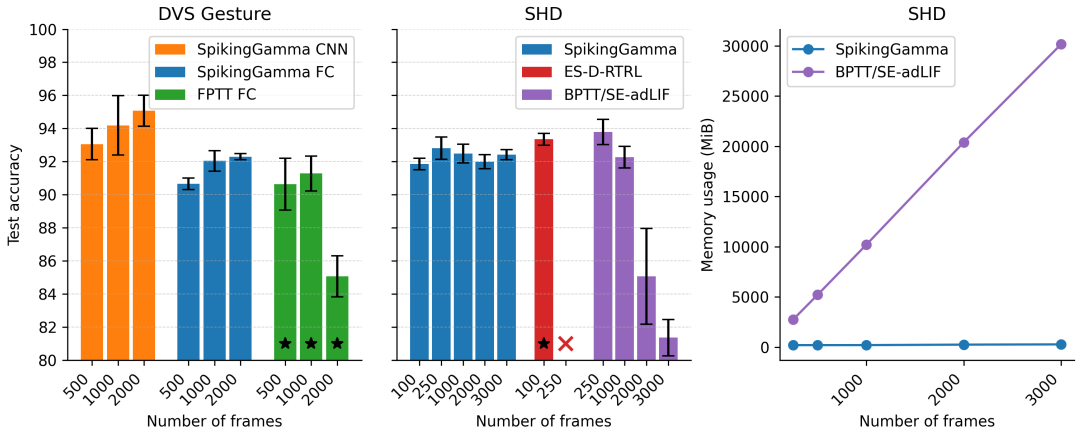


Figure 8: Effect of increasing the number of frames on test accuracy and memory usage. The "x" symbol refers to chance level performance. Bars marked with an asterisk (\*) correspond to peak test accuracy observed during training, while the other results correspond to test accuracy obtained after completing training. Detailed results, including the performance in between 100 and 250 frames for ES-D-RTRL, can be found in Section A.1 (Appendix). Peak results for SpikingGamma are provided in Section A.2 (Appendix). In addition to our results, (Yin et al., 2023) reports degrading test accuracy for LSTM, ASRNN, and LTC neurons on DVS Gesture trained with BPTT as the number of frames increases, becoming evident between 200 and 500 frames.

tic power-law-like pattern (Figure 7). This suggests that our model captures temporal information in a manner consistent with biological neural representations of time.

**Temporal precision** Increasing the temporal resolution results in longer sequences, which by itself has a strongly detrimental effect on BPTT performance (Yin et al., 2023). Moreover, BPTT/RTRL approximations often perform well only after extensive hyperparameter tuning (Xue et al., 2024) and studies of achievable temporal precision are lacking except for comparatively easy datasets such as DVS Gesture (Wang et al., 2024; Yin et al., 2023), which is known to contain limited temporal structure (Chen et al., 2025). Here, we perform a more extensive study by evaluating performance at finer temporal resolutions for both DVS Gesture and SHD. To keep the temporal dynamics consistent, we scale the bucket transfer rate by the same factor as the timestep change. To further broaden the comparison, we additionally train with a larger number of frames using publicly available implementations of FPTT, ES-D-RTRL, and SE-adLIF.

In Figure 8, we see that as the number of frames increases, SpikingGamma maintains stable accuracy on DVS Gesture, even improving slightly, while FPTT degrades sharply. On SHD, ES-D-RTRL completely collapses, and SE-adLIF also deteriorates substantially, whereas SpikingGamma maintains performance. Memory usage remains low and theoretically constant over time, increasing slightly in practice due to software overhead, while BPTT-based methods scale linearly with the number of frames.

**Sparsity** SpikingGamma SNNs can theoretically achieve highly efficient spike-coding, as shown by the coincidence detection task, by keeping most of the dynamics subthreshold and using spike timing codes rather than relying solely on rate codes. This is similar to how delays or adaptive neurons enable efficient neural codes. When applying gain loss

on SHD, we reach a spike density comparable to competitive methods (5 to 6 spikes/neuron/sample (Deckers et al., 2024) with little decrease in accuracy), as shown in Figure A3 (Appendix). However, because the SHD data is essentially rate-coded (Cramer et al., 2020), its potential for sparsity is inherently limited (Yu et al., 2025). For datasets with richer temporal structures, we expect larger gains in sparsity.

## 5 Discussion and Conclusion

We introduced the SpikingGamma model, an online training approach for SNNs that supports direct error backpropagation without surrogate gradients, thereby eliminating the approximation errors that limit existing online methods. As a result, SpikingGamma enables learning at finer temporal resolutions than previously possible while preserving the ability to capture long-range and complex temporal dependencies. By maintaining information through subthreshold dynamics, it further encourages sparse spike coding, making the resulting models more compatible with the communication constraints of neuromorphic hardware. These advantages bring SNNs closer to large-scale deployment and suggest SpikingGamma models as a foundation for energy-efficient neuromorphic AI.

Even higher levels of sparsity could be achieved by further exploiting SpikingGamma’s ability to learn complex temporal feature detectors at both the neuron and synapse level. Many large-scale benchmarks, however, are defined by rate-code models, which makes it difficult to evaluate and benefit from sparse temporal coding strategies (Yu et al., 2025). Benchmarks that target temporal coding could therefore better reveal the efficiency gains enabled by SpikingGamma. Finally, with modern AI dominated by feedforward network architectures such Transformers, similar modifications to SpikingGamma seem promising to achieve scalable and powerful deep SNNs for sequence learning.

## Acknowledgements

Roel Koopman is funded by the Dutch Research Council under Grant agreement KICH1.ST04.22.021. Sander Bohté is supported by NWO-NWA grant NWA.1292.19.298. Sebastian Otte acknowledges support from the Alexander von Humboldt Foundation (Feodor Lynen Research Fellowship) during the early phase of this work.

## References

Amir, A., Taba, B., Berg, D., Melano, T., McKinstry, J., Di Nolfo, C., Nayak, T., Andreopoulos, A., Garreau, G., Mendoza, M., et al. A low power, fully event-based gesture recognition system. In *Proceedings of the IEEE conference on computer vision and pattern recognition*, pp. 7243–7252, 2017.

Ba, J. L., Kiros, J. R., and Hinton, G. E. Layer normalization. *arXiv preprint arXiv:1607.06450*, 2016.

Baek, S. and Lee, J. Snn and sound: a comprehensive review of spiking neural networks in sound. *Biomedical Engineering Letters*, 14(5):981–991, 2024.

Baronig, M., Ferrand, R., Sabathiel, S., and Legenstein, R. Advancing spatio-temporal processing through adaptation in spiking neural networks. *Nature Communications*, 16: 5776, 2025.

Bohnstingl, T., Woźniak, S., Pantazi, A., and Eleftheriou, E. Online spatio-temporal learning in deep neural networks. *IEEE Transactions on Neural Networks and Learning Systems*, 34(11):8894–8908, 2022.

Bohte, S. M. Error-backpropagation in networks of fractionally predictive spiking neurons. In *International conference on artificial neural networks*, pp. 60–68. Springer, 2011.

Carr, C. and Konishi, M. A circuit for detection of interaural time differences in the brain stem of the barn owl. *Journal of Neuroscience*, 10(10):3227–3246, 1990.

Chen, X., Ma, C., Wu, Y., Tan, K., and Wu, J. Neuromorphic sequential arena: A benchmark for neuromorphic temporal processing. In *The 34th International Joint Conference on Artificial Intelligence (IJCAI'25)*, 2025.

Cramer, B., Stradmann, Y., Schemmel, J., and Zenke, F. The heidelberg spiking data sets for the systematic evaluation of spiking neural networks. *IEEE Transactions on Neural Networks and Learning Systems*, 33(7):2744–2757, 2020.

Cramer, B., Billaudelle, S., Kanya, S., Leibfried, A., Grübl, A., Karasenko, V., Pehle, C., Schreiber, K., Stradmann, Y., Weis, J., et al. Surrogate gradients for analog neuromorphic computing. *Proceedings of the National Academy of Sciences*, 119(4):e2109194119, 2022.

Dampfhofer, M., Mesquida, T., Valentian, A., and Anghel, L. Are snns really more energy-efficient than anns? an in-depth hardware-aware study. *IEEE Transactions on Emerging Topics in Computational Intelligence*, 7(3):731–741, 2022.

De Vries, B. and Principe, J. C. The gamma model—a new neural model for temporal processing. *Neural networks*, 5 (4):565–576, 1992.

Deckers, L., Van Damme, L., Van Leeuwijk, W., Tsang, I. J., and Latré, S. Co-learning synaptic delays, weights and adaptation in spiking neural networks. *Frontiers in Neuroscience*, 18:1360300, 2024.

Drew, P. J. and Abbott, L. F. Models and properties of power-law adaptation in neural systems. *Journal of neurophysiology*, 96(2):826–833, 2006.

Eshraghian, J. K., Ward, M., Neftci, E. O., Wang, X., Lenz, G., Dwivedi, G., Bennamoun, M., Jeong, D. S., and Lu, W. D. Training spiking neural networks using lessons from deep learning. *Proceedings of the IEEE*, 111(9):1016–1054, 2023.

Gerstner, W. and Kistler, W. M. *Spiking neuron models: Single neurons, populations, plasticity*. Cambridge university press, 2002.

Hagenaars, J. J., Paredes-Vallés, F., Bohté, S. M., and De Croon, G. C. Evolved neuromorphic control for high speed divergence-based landings of mavs. *IEEE Robotics and Automation Letters*, 5(4):6239–6246, 2020.

Hammouamri, I., Khalfaoui-Hassani, I., and Masquelier, T. Learning delays in spiking neural networks using dilated convolutions with learnable spacings. In *The Twelfth International Conference on Learning Representations*, 2024.

Ioffe, S. and Szegedy, C. Batch normalization: Accelerating deep network training by reducing internal covariate shift. In *International conference on machine learning*, pp. 448–456. pmlr, 2015.

Kag, A. and Saligrama, V. Training recurrent neural networks via forward propagation through time. In *International Conference on Machine Learning*, pp. 5189–5200. PMLR, 2021.

Kaiser, J., Mostafa, H., and Neftci, E. Synaptic plasticity dynamics for deep continuous local learning (decolle). *Frontiers in Neuroscience*, 14:424, 2020.

Kim, Y. and Panda, P. Revisiting batch normalization for training low-latency deep spiking neural networks from scratch. *Frontiers in neuroscience*, 15:773954, 2021.

Ko, J., Kwon, D., Hwang, J., Lee, K.-H., Oh, S., Kim, J., Im, J., Koo, R.-H., Kim, J.-J., and Lee, J.-H. Snnsim: Investigation and optimization of large-scale analog spiking neural networks based on flash memory devices. *Advanced Intelligent Systems*, 6(4):2300456, 2024.

Koopman, R., Yousefzadeh, A., Shahsavari, M., Tang, G., and Sifalakis, M. Exploring the limitations of layer synchronization in spiking neural networks. *Transactions on Machine Learning Research*, 2025. ISSN 2835-8856.

Laurent, C., Pereyra, G., Brakel, P., Zhang, Y., and Bengio, Y. Batch normalized recurrent neural networks. In *2016 IEEE International Conference on Acoustics, Speech and Signal Processing (ICASSP)*, pp. 2657–2661. IEEE, 2016.

Li, Y., Yin, R., Kim, Y., and Panda, P. Efficient human activity recognition with spatio-temporal spiking neural networks. *Frontiers in Neuroscience*, 17:1233037, 2023.

Li, Y., Zhao, F., Zhao, D., and Zeng, Y. Directly training temporal spiking neural network with sparse surrogate gradient. *Neural Networks*, 179:106499, 2024.

Liu, Y., Tiganj, Z., Hasselmo, M. E., and Howard, M. W. A neural microcircuit model for a scalable scale-invariant representation of time. *Hippocampus*, 29(3):260–274, 2019.

Ludvig, E. A., Sutton, R. S., and Kehoe, E. J. Stimulus representation and the timing of reward-prediction errors in models of the dopamine system. *Neural computation*, 20(12):3034–3054, 2008.

Maass, W. Networks of spiking neurons: the third generation of neural network models. *Neural networks*, 10(9):1659–1671, 1997.

Martínez, F. S., Casas-Roma, J., Subirats, L., and Parada, R. Spiking neural networks for autonomous driving: A review. *Engineering Applications of Artificial Intelligence*, 138:109415, 2024.

Mészáros, B., Knight, J. C., and Nowotny, T. Efficient event-based delay learning in spiking neural networks. *Nature Communications*, 16(1):10422, 2025.

Neftci, E. O., Mostafa, H., and Zenke, F. Surrogate gradient learning in spiking neural networks: Bringing the power of gradient-based optimization to spiking neural networks. *IEEE Signal Processing Magazine*, 36(6):51–63, 2019.

Quintana, F. M., Perez-Peña, F., Galindo, P. L., Neftci, E. O., Chicca, E., and Khacef, L. Etlp: event-based three-factor local plasticity for online learning with neuromorphic hardware. *Neuromorphic Computing and Engineering*, 4(3):034006, 2024.

Rombouts, J. and Bohte, S. Fractionally predictive spiking neurons. *Advances in Neural Information Processing Systems*, 23, 2010.

Shimbo, A., Izawa, E.-I., and Fujisawa, S. Scalable representation of time in the hippocampus. *Science Advances*, 7(6):eabd7013, 2021. Published at <https://www.science.org/doi/10.1126/sciadv.abd7013>, licensed under CC BY-NC 4.0.

Summe, T. M., Schaefer, C. J., and Joshi, S. Estimating post-synaptic effects for online training of feed-forward snns. In *2024 International Conference on Neuromorphic Systems (ICONS)*, pp. 264–271. IEEE, 2024.

Sutskever, I. and Hinton, G. Temporal-kernel recurrent neural networks. *Neural Networks*, 23(2):239–243, 2010.

Van Den Oord, A., Dieleman, S., Zen, H., Simonyan, K., Vinyals, O., Graves, A., Kalchbrenner, N., Senior, A., Kavukcuoglu, K., et al. Wavenet: A generative model for raw audio. *arXiv preprint arXiv:1609.03499*, 12:1, 2016.

Wang, C., Dong, X., Ji, Z., Jiang, J., Liu, X., and Wu, S. Brainscale, enabling scalable online learning in spiking neural networks. *bioRxiv*, pp. 2024–09, 2024.

Xiao, M., Meng, Q., Zhang, Z., He, D., and Lin, Z. Online training through time for spiking neural networks. *Advances in neural information processing systems*, 35:20717–20730, 2022.

Xue, L., Liu, H., Wang, J., and Qu, H. Reasonable gradients for online training algorithms in spiking neural networks. In *ECAI 2024*, pp. 2709–2716. IOS Press, 2024.

Yin, B., Corradi, F., and Bohté, S. Accurate online training of dynamical spiking neural networks through forward propagation through time. *Nature Machine Intelligence*, 5:1–10, 05 2023. doi: 10.1038/s42256-023-00650-4.

Yoon, Y. C. Lif and simplified srm neurons encode signals into spikes via a form of asynchronous pulse sigma-delta modulation. *IEEE transactions on neural networks and learning systems*, 28(5):1192–1205, 2016.

Yu, Z., Sun, P., and Goodman, D. F. Beyond rate coding: Surrogate gradients enable spike timing learning in spiking neural networks. *arXiv preprint arXiv:2507.16043*, 2025.

Zambrano, D., Nusselder, R., Scholte, H. S., and Bohté, S. M. Sparse computation in adaptive spiking neural networks. *Frontiers in neuroscience*, 12:987, 2019.

Zenke, F. and Vogels, T. P. The remarkable robustness of surrogate gradient learning for instilling complex function in spiking neural networks. *Neural computation*, 33(4):899–925, 2021.

Zhang, B. and Sennrich, R. Root mean square layer normalization. *Advances in neural information processing systems*, 32, 2019.

Zhou, C., Zhang, H., Yu, L., Ye, Y., Zhou, Z., Huang, L., Ma, Z., Fan, X., Zhou, H., and Tian, Y. Direct training high-performance deep spiking neural networks: a review of theories and methods. *Frontiers in Neuroscience*, 18:1383844, 2024.

## A Extended results

### A.1 Performance comparison when increasing number of frames

For the reproduced works, we examined how time constants were applied and whether they required adjustment when the number of frames (and thus the timestep size) changed. For FPTT, ES-D-RTRL, and SE-adLIF, the time constants are trainable. We observed no performance improvements from modifying their bounds or initialization.

Table A1: Test accuracy for models trained on DVS Gesture. \*Reproduced from <https://github.com/byin-cwi/sFPTT>. No annotation means the number is from the original work.

Frames	SpikingGamma (CNN)	SpikingGamma (FC)	FPTT
500	$93.06 \pm 0.94$	$90.66 \pm 0.36$	$90.64 \pm 1.56$
1000	$94.19 \pm 1.79$	$92.05 \pm 0.62$	$91.28 \pm 1.05$
2000	$95.08 \pm 0.93$	$92.30 \pm 0.18$	$85.07 \pm 1.24^*$

Table A2: Test accuracy for models trained on SHD. \*Reproduced from <https://github.com/chaobrain/brainscale-exp-for-snns> (commit 11720f5). The number of epochs was reduced from 100 to 30. For 250+ frames, ES-D-RTRL no longer converges, see Figure A1 for transition and collapse from 100 to 300 frames. Therefore, we did not reproduce for 1000 or more frames. \*\*Reproduced from <https://github.com/IGITUGraz/SE-adlif>. No annotation means the number is from the original work.

Frames	SpikingGamma	ES-D-RTRL	BPTT/SE-adLIF
100	$91.86 \pm 0.34$	$93.35 \pm 0.36$	-
250	$92.81 \pm 0.68$	$4.5^*$	$93.79 \pm 0.76$
1000	$92.49 \pm 0.57$	-	$92.26 \pm 0.65^{**}$
2000	$91.99 \pm 0.43$	-	$85.06 \pm 2.89^{**}$
3000	$92.42 \pm 0.31$	-	$81.36 \pm 1.11^{**}$

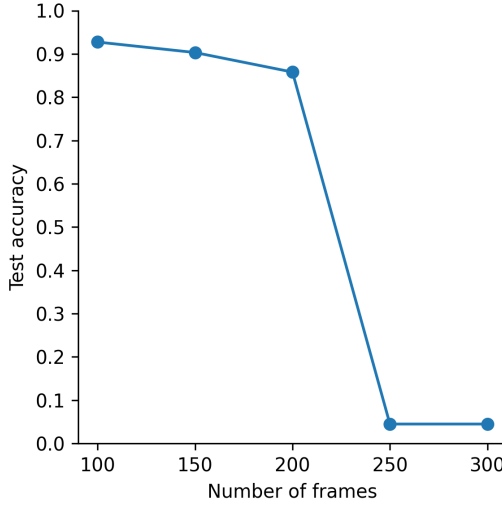


Figure A1: Test accuracy (best over all epochs) for ES-D-RTRL (reproduced) trained on SHD from 100 to 300 frames. The accuracy for 250 frames was verified over 3 independent training sessions.

### A.2 Peak test accuracy during training

A common practice in prior work is to select the peak test performance observed during training, effectively using the test set to guide model selection. This introduces test set information into the training process and can lead to fitting on the test set,

thereby overestimating generalization performance. To avoid this issue, we did not adopt this practice. However, to ensure a fair comparison with related works that did use this strategy, in Table A3 we additionally report the peak test performance achieved over the course of training (with the number of epochs increased to 30 for SHD/SSC and to 150 for DVS Gesture). As expected, these numbers are slightly higher, but the overall trends remain consistent.

Table A3: Peak test accuracies achieved during training.

Task	Frames	Accuracy $\pm$ std
DVS Gesture (CNN)	500	95.58 $\pm$ 0.18
	1000	96.21 $\pm$ 0.31
	2000	96.08 $\pm$ 0.18
DVS Gesture (FC)	500	92.80 $\pm$ 0.62
	1000	93.31 $\pm$ 0.18
	2000	93.81 $\pm$ 0.18
SHD	100	92.64 $\pm$ 0.27
	250	93.55 $\pm$ 0.48
	1000	93.18 $\pm$ 0.34
	2000	92.61 $\pm$ 0.39
	3000	93.31 $\pm$ 0.24
SSC	250	75.91 $\pm$ 0.54

#### A.2.1 Clarifying reported test accuracy for DECOLLE

Since the original work on DECOLLE in (Kaiser et al., 2020) was ambiguous about whether it reported peak or final epoch test accuracy, we reproduced their results using the original code (<https://github.com/nmi-lab/decolle-public>) to clarify this point. Across four independent runs, we obtained a peak test accuracy of  $95.70 \pm 0.47$  and a final epoch test accuracy of  $94.19 \pm 0.94$ . The peak accuracy aligns much more closely with the reported value of  $95.54 \pm 0.16$ , indicating that the original paper most likely reported peak test accuracy rather than final epoch accuracy.

### A.3 Effect of introducing a variable threshold

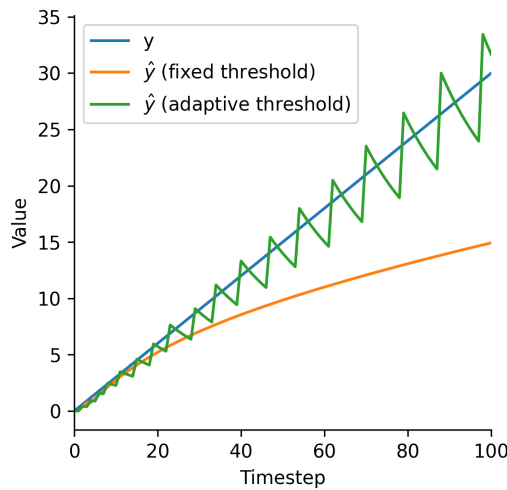


Figure A2: A demonstration showing that, without adaptive thresholding,  $\hat{y}$  is unable to accurately estimate higher values of  $y$ , whereas the use of adaptive thresholding enables  $\hat{y}$  to effectively estimate these higher values.

## A.4 Ablation study on SHD

To gather more insight into the effects of normalization, activation, and hyperparameters, we performed an ablation study on SHD. We used the same experimental setup as for our best-performing model, but introduced the modifications listed in Tables A4 and A5.

During our experiments, the neuron signal was first normalized using layer normalization and then rectified. As shown in Table A4, removing the ReLU activation used to compute the neuron signal  $y$  leads to a clear drop in performance. This is expected, as negative neuron signal values cannot be represented by spikes in our method, resulting in a mismatch between the signal  $y$  and its estimate  $\hat{y}$ .

Additionally, altering or removing this normalization can have substantial impact on accuracy. RMS normalization (Zhang & Sennrich, 2019) performs similarly to layer normalization, which is expected since both normalize using the same underlying statistics. In contrast, batch normalization (Ioffe & Szegedy, 2015) completely fails. This aligns with previous findings that batch normalization is difficult to apply to the hidden-to-hidden transitions of RNNs (Laurent et al., 2016). Batch normalization through time (Kim & Panda, 2021) was designed to better capture temporal characteristics than standard batch normalization, and our results confirm this, though its performance still lags behind layer and RMS normalization. Finally, omitting normalization altogether yields mixed results: when bucket weights are assigned to neurons, performance is poor, but assigning them to synapses improves results, though still with much higher variance. In summary, properly normalizing neuron signal dynamics is essential for stable training and good performance when scaling to a more complex task like SHD.

Table A4: Ablation study results for SHD.

Ablated	Accuracy $\pm$ std
No normalization, bucket weights on neuron	$50.83 \pm 9.10$
No normalization, bucket weights on synapse	$88.31 \pm 3.15$
RMS normalization	$92.54 \pm 0.63$
Batch normalization	$16.59 \pm 3.28$
Batch normalization through time	$90.57 \pm 0.60$
No ReLU	$85.38 \pm 1.37$

In Section 3.3, we introduced the standard method for initializing the bucket transfer rates. This approach is based on the idea that a well-chosen power-law-like shape (given by the sum of all buckets) is most effective at retaining information. We test this hypothesis by using different shapes and rates, as shown in Table A5. The results confirm that a power-law sum of responses, decaying over an appropriate time interval, yields the best performance, while all other response shapes underperform.

Table A5: Results from experiments with alternative kernel parameters and shapes. The "Power-law" shape type refers to the default initialization method as introduced in section 3.3, while "Fixed rate" refers to an alternative scheme where  $\alpha_k$  is fixed to one value (given as "Rate") for all  $K$  kernels. The visualized neuron responses shows the sum of all kernel responses, with on x-axis 100 timesteps and on y-axis values from 0 to 1.

Shape type	Rate / $F$	$K$	Neuron response	Accuracy
Fixed rate	0.82	10		$75.45 \pm 1.16$
Fixed rate	0.15	10		$67.04 \pm 1.48$
Power-law	1.00	1		$32.82 \pm 1.09$
Power-law	0.00	1		$22.14 \pm 4.71$
Power-law	0.90	10		$84.49 \pm 0.88$
<b>Power-law</b>	<b>0.15</b>	<b>10</b>		<b><math>92.81 \pm 0.68</math></b>
Power-law	0.01	10		$87.52 \pm 0.38$

We also experimented with the gain–loss constant to achieve sparsity, as shown in Figure A3. Setting the constant to 0.1 resulted in a significant increase in sparsity with little to no degradation in accuracy. Increasing the constant further continued to improve sparsity, but at the cost of progressively larger accuracy losses.

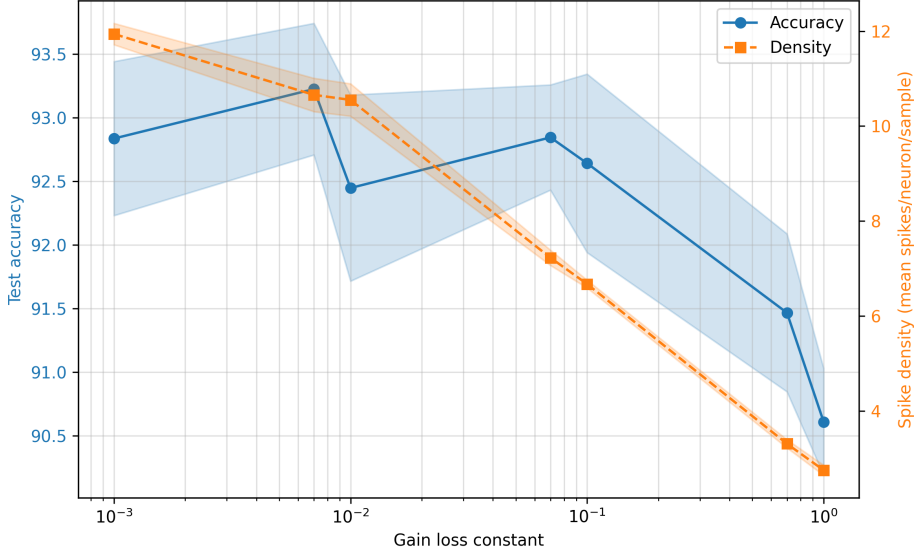


Figure A3: Effect of the gain-loss constant on accuracy and spike density (shown as mean  $\pm$  std). The spike density is computed using Eq. (B3).

## B Details on the experimental setup

### B.1 Datasets

The Spiking Heidelberg Digits (SHD) and Spiking Speech Commands (SSC) datasets both consist of auditory recordings. Each recording was converted into spike trains using a biologically inspired cochlear model, capturing fine-grained temporal structure in the audio (Cramer et al., 2020). The SHD dataset contains 8156 training and 2264 test samples for 20 spoken digits. The SSC dataset contains 75466 training, 9981 validation, and 20382 test samples for 35 spoken digits. We included the validation samples in the training set (and did no validation during training). For both datasets, the 700-channel cochlear outputs are downsampled to 140 channels to reduce input dimensionality.

The DVS Gesture dataset (Amir et al., 2017) contains event-based visual recordings of 11 hand and arm gestures captured using a DVS camera. It includes 1176 training and 288 test samples. The original  $128 \times 128$  event frames are downsampled to  $32 \times 32$  by summing up events in a  $4 \times 4$  window.

To prepare the event streams from the datasets for model input, the timestamps are discretized into time-bins along the temporal axis. All events falling within the same time-bin are accumulated at their corresponding spatial indices, producing a sequence of frames. These frames are then fed to the model as inputs at successive discrete timesteps.

For computing the mean and standard deviation of the reported accuracies, we repeated the experiments with SHD and SSC 5 times, and with DVS Gesture 3 times.

Table B1: Network architecture and hyperparameters. The architecture is given as [neurons in hidden layers  $\times$  number of hidden layers] if fully-connected. Whenever we change the number of frames / the timestep size from the values mentioned above, we scale the bucket transfer rate by the same factor as the timestep size change to keep the temporal dynamics consistent. \*Times  $K$  per layer upward starting from the output towards the input.

	SHD	SSC	DVS Gesture
Architecture	[256 $\times$ 3]	[512 $\times$ 3]	B.2.1
Timestep size	3.6 ms	3.6 ms	3 ms
Number of frames	250	250	2000
Batch size	32	32	64
Epochs	25	25	100
Initial learning rate	1e-3*	1e-3*	1e-3
Learning rate schedule	Step	Step	None
Schedule step size	10	10	
Schedule step gamma	0.1	0.1	
Minimum threshold $\vartheta_0$	0.2	0.2	0.2
Number of buckets $K$	10	7	10
Bucket transfer rate $F$	0.15	0.15	0.05
Dropout	0.1	0.1	0
Loss function	CE	CE warm-up (B.3.1)	CE

## B.2 Network architectures and hyperparameters

### B.2.1 DVS Gesture model architecture

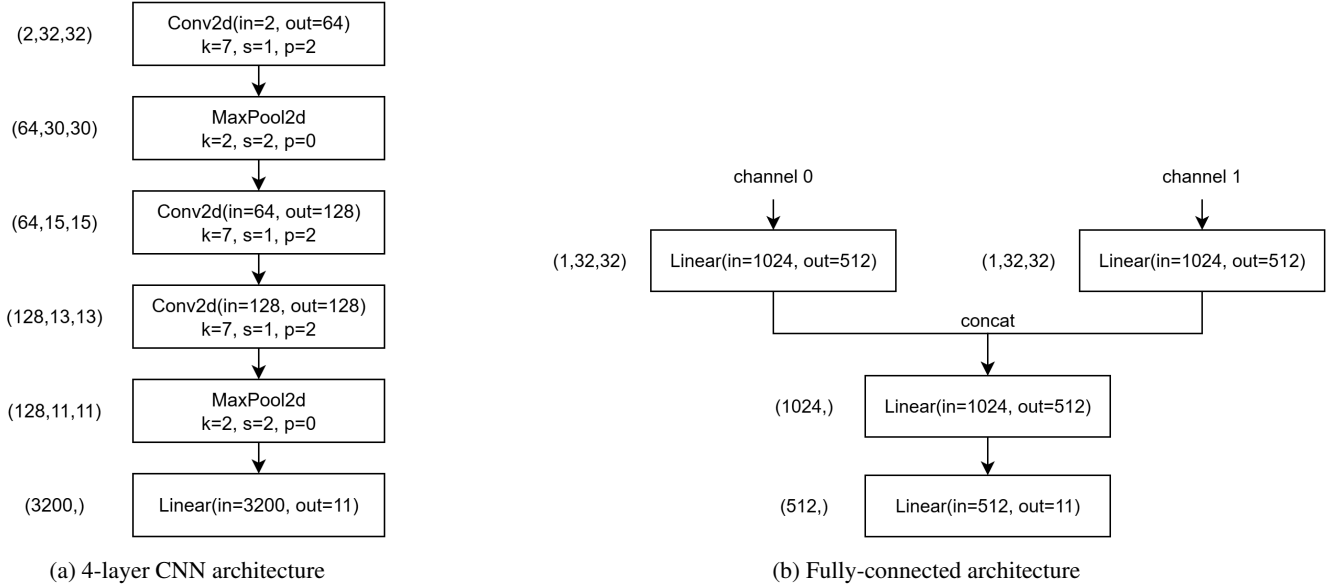


Figure B1: (a) shows the 4-layer CNN architecture used for DVS Gesture (similar to what was used for DECOLLE in (Kaiser et al., 2020)). (b) shows the fully-connected architecture (similar to what was used for FPTT in (Yin et al., 2023)). In both Figures, neuron layers (that include normalization and dropout if applicable) are omitted; they are placed after each Conv2d or Linear layer.

## B.3 Performance metrics

### B.3.1 CE warm-up loss

For SSC, there is a delay in sample onset. This can be problematic when training online. To improve performance, we introduce a custom loss function that trains to mute the output at the start of the sample. It interpolates between MSE to zero and CE loss

using a time-dependent weight:

$$L(t) = \beta(t) \cdot L^{\text{MSE}}(\hat{y}_{\text{out}}(t), 0) + (1 - \beta(t)) \cdot L^{\text{CE}}(y_{\text{out}}(t), y_{\text{true}}(t)) \quad (\text{B1})$$

where

$$\beta(t) = \beta_0 \cdot (\beta_{\text{decay}})^t. \quad (\text{B2})$$

with  $\beta_{\text{decay}} = 0.99$ .

### B.3.2 Spike density

$$\text{spike density} = \frac{1}{N_{\text{samples}} \cdot N_{\text{neurons}}} \sum_{i=1}^{N_{\text{samples}}} N_{\text{spikes}}[i] \quad (\text{B3})$$

where  $N_{\text{samples}}$  is the dataset size,  $N_{\text{neurons}}$  is the total number of neurons in the hidden layers, and  $N_{\text{spikes}}[i]$  is the spike count recorded during the inference of the  $i$ -th sample.